Selecting the molecular components of a pitch to produce a hard carbon anode with a high sodium storage capacity

Wang Peixiang[1], Wang Bin[1,*], Li Yuqi[1], Wang Wanli[1], Sun Yi[1], Song Longsen[1], Liu Chenhao[1], P. Iamprasertkun[2], Hu Han[1,*], Wu Mingbo[1]

(1. *State Key Laboratory of Heavy Oil Processing*, *Institute of New Energy*, *College of Chemistry and Chemical Engineering*, *China University of Petroleum (East China)*, *Qingdao* 266580, *China*;
2. *Sirindhorn International Institute of Technology*, *Thammasat University*, *Pathum Thani* 12150, *Thailand*)

Abstract: Pitch is an excellent precursor for the production of hard carbon, with pre-oxidation crucial process in the fabrication. The structural changes in the different molecular components of pitch during thermochemical treatment are a key factor in determining the sodium-ion storage of pitch-based hard carbon anodes. We investigated the effects of the different molecular structures in the asphaltene precursor, including aromatic rings and aliphatic chains, on the sodium-ion storage behavior of the resulting carbon. We found that polar oxygen functional groups limit the steric hindrance caused by the aromatic rings in pitch, and thus facilitate the introduction of cross-linked structures. During high-temperature carbonization, aromatic rings form a rigid carbon framework that prevents the rearrangement of ordered carbon layers, leading to a short-range disordered carbon structure and promotes the production of closed pores. For example, a material prepared from asphaltene, which contains a large number of oxygen-containing functional groups and macromolecular aromatic rings, using pre-oxidation at 300 °C and carbonization at 1200 °C had a reversible capacity of 316.7 mAh g^{-1} when used as the anode for sodium ion batteries. Our research provides a theoretical basis for the selection of raw materials for the development of high-quality pitch-based hard carbons.

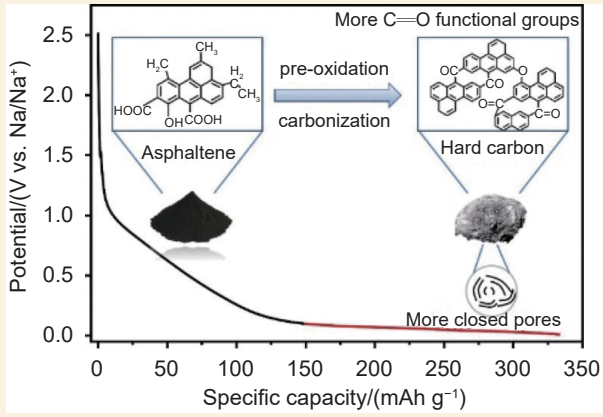

Key words: Energy storage; Asphaltene; Pre-oxidation; Hard carbon; Sodium-ion batteries

1 Introduction

Concerns regarding environmental pollution and energy depletion are propelling the expansion of renewable energy, leading to an increased demand for advanced energy storage solutions. Sodium-ion batteries (SIBs) present a viable alternative to widely used lithium-ion batteries (LIBs) due to their lower cost and enhanced safety profile. However, the development of high-performance, cost-effective, and high-stability anode materials still remains a significant challenge for the commercialization of SIBs[1–3]. Hard carbon is distinguished among anode materials owing to its abundance, low cost, and wide operating voltage range[4–5].

Hard carbon materials are generally synthesized through the pyrolysis of various precursors, including biomass[6], fossil fuels[7], organic small molecules[8], and polymer[9]. Petroleum pitch, a byproduct of the petroleum industry, is cost-effective and has a higher carbon content compared with other precursors, contributing to reducing electrode expenses[10]. However, not only the provenance or batch of pitch gives rise to pronounced compositional variations, but the carbon derived from the direct carbonization of petroleum pitch tends to be highly graphitized with small inter-

Received: February 12, 2025
Revised: February 25, 2025
Accepted: February 25, 2025

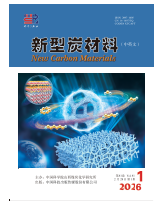

layer spacings, leading to limited sodium-ion storage performance. Converting pitch into hard carbon materials requires introduction of additional cross-linking structures to prevent its melting during high-temperature carbonization. This approach prevents the formation of viscous liquid intermediates and effectively suppresses the rearrangement of carbon layers. Extensive studies have investigated a varity of modification methods for petroleum pitch, such as potassium permanganate treatment[11], acid treatment[12], template interference[13] and co-carbonization[14]. Nonetheless, these methods often involve complex processes that are not suitable for large-scale industrial production. The pre-oxidation process entails the thermal treatment of pitch in an atmosphere rich in air or oxygen, facilitating the incorporation of oxygen-containing functional groups without the necessity for dopants or intricate procedures. This method lends itself to automation, making it suitable for large-scale production, thereby significantly lowering material production costs and improving manufacturing efficiency.

Petroleum pitch is complex and can be divided into resins, asphaltenes, saturates, and aromatics[15]. During the pyrolysis process, the saturates primarily volatilize, generating gaseous products with minimal impact on the carbon material structure. Aromatics and resins play a crucial role in forming graphitic nanodomains, although their bulky steric effects hinder the introduction of oxygen-containing functional groups. The asphaltene fraction is generally regarded as the primary component responsible for constructing the carbon framework due to its high molecular weight and complex aromatic structures[16]. During the pre-oxidation process, some $-CH_n$ function groups in the aliphatic side chains and aromatic structures undergo dehydrogenation and condensation, while others crosslink and condense with oxygen from the air to form aromatic ethers, as well as aromatic aldehydes, ketones, or esters[17]. In the subsequent carbonization process, the three-dimensional cross-linking structures formed by O=C—O convert the petroleum pitch into solid-phase carbon, suppressing carbon layer rearrangement[17]. The gases produced during pyrolysis further disrupt the carbon structure, facilitating the formation of ultra-micropores or closed pores. However, in practical research, petroleum pitches with different components often exhibit varying electrochemical storage behaviors and reversible capacities under the same heat treatment conditions[18]. This suggests that structural differences in the pitch components, particularly key components, have a significant effect on the properties of the final hard carbon. Similar phenomenon has been observed in lignin-derived hard carbon, where the structural differences between aromatic rings and aliphatic chains significantly influence the formation of closed pores[5]. Current research on petroleum pitch-derived hard carbon primarily focuses on modifying the entire raw material[19]. However, the influence of various molecular constituents of raw pitch on the structure, functional group, and electrochemical performance of hard carbon remains predominantly unexamined.

In this study, we investigated the influence of aromatic structures and aliphatic chains in asphaltenes on the critical structures of hard carbon (surface defects and closed pores) under pre-oxidation treatment, using n-heptane-extracted asphaltenes. Molecular structure characterization, including nuclear magnetic resonance (NMR), X-ray diffraction (XRD), and X-ray photoelectron spectroscopy (XPS), revealed that air pre-oxidation primarily affects specific structural features, such as aliphatic carbon chains and oxygen-containing functional groups. The introduction of cross-linking groups (C=O, O=C—O) further influences the closed pores in hard carbon, through the careful analysis of graphite microcrystal size. Thus, the steric hindrance effect of aromatics facilitates the production of closed pore structures. The Z2 materials with aromatic structures and polar oxygen-containing functional groups leading to an optimized hard carbon (Z2-300-1200) with a high reversible capacity of 316.7 mAh g^{-1}. Our research provides a theoretical foundation for the selection of upstream raw materials aiming at the development of high-quality pitch-derived hard carbons.

2 Experimental

2.1 Material preparation

China national petroleum corporation (CNPC) supplied the three types of pitch used in this study. Z1 and Z3 were obtained by solvent extraction and thermal polycondensation of vacuum residue produced after crude oil distillation. Z2 was a coated pitch created through a sequence of processes comprising ethylene tar selection, purification, settling, oxidation, secondary distillation. To eliminate the influence of other components (saturates, aromatics, resins) in the pitches, we employed n-Heptane extraction to isolate asphaltenes. We stirred a mixture of pitch and n-heptane at a ratio of 1∶30 overnight. According to the principle of "like dissolves like", the nonpolar components in the pitch dissolved in n-Heptane, leaving the insoluble asphaltene. We dried the asphaltene in an oven at 100 °C for 12 h to eliminate any remaining n-heptane. We then placed a portion of the asphaltene in a tube furnace and heated it at a rate of 5 °C min^{-1} to 300 °C, holding it for 10 h to allow sufficient contact with oxygen and introduce oxygen-containing functional groups. Finally, we ground the pre-oxidized asphaltene into powder and subjected it to high-temperature carbonization at 1200 °C for 2 h, at a heating rate of 5 °C min^{-1}, to produce asphaltene-derived hard carbons. We synthesized three hard carbon materials, designated as Z1-300-1200, Z2-300-1200 and Z3-300-1200, by subjecting the 2 remaining asphaltenes to an identical treatment process.

2.2 Material characterization

^{13}C solid-state NMR were recorded on a Bruker Avance II 400 spectrometer. The crystallographic structure is measured by X-ray diffraction (XRD) (X'Pert PRO MPD, Holland). XPS was collected using the Escalab 250XI instrument manufactured by Thermo Fisher Scientific. Microstructures were analyzed utilizing scanning electron microscopy (SEM) with the model JSM-9600F. The accelerating voltage is 5.0 kV. High-resolution transmission electron microscopy (HRTEM) images were obtained using the JEM-2100UHR. Raman spectra were measured on a Thermo Scientific Raman Spectrometer, employing a laser wavelength of 532 nm. Electron paramagnetic resonance (EPR) spectra were recorded using an X-band Bruker EMX-PLUS spectrometer. Small-angle X-ray scattering (SAXS) measurements were collected using the Anton Paar SAXS point 2.0. The pore structures were examined on a Micromeritics TriStar II 3020 analyzer using N_2 /CO_2 as an adsorbent.

2.3 Electrode fabrication and electrochemical characterization

The active material, Super P, and polyvinylidene difluoride (PVDF) were mixed in N-methyl-2-pyrrolidinone (NMP) in the ratio of 8∶1∶1 and then coated on copper foil and dried in a vacuum oven at 60 °C for 12 h. The dried electrode sheets were then cut into 12 mm pieces and assembled in an argon-filled glove box to form a CR2032 (Canrd) button cell (H_2O, O_2 < 1.0×10^{-4}). 1 mol $NaClO_4$ in diethyl carbonate (DEC)/vinyl carbonate (EC) (*v*/*v*=1∶1, with 5% FEC) (Saios) was served as the electrolyte. CR2032 full cell with Z2-300-1200 as the negative electrode, PB (Prussian blue) as the positive electrode. The negative/positive capacity ratio (N/P ratio) was positioned at 0.75. Cycling performance, rate performance, and galvanostatic intermittent titration technique (GITT) tests were recorded using the NEWWARE BTS-5V measurement system. Electrochemical impedance spectroscopy (EIS) and cyclic voltammetry (CV) were determined using the LVIUM-SATA electrochemical workstation. The frequency range of EIS was setted in the range from 100 kHz to 1 Hz.

3 Results and discussion

3.1 Structural characterization of asphaltene feedstocks

The n-Heptane was used to extract the asphaltenes, and due to the principle of like dissolves like, the saturated portion, aromatic portion, and resins portion of petroleum pitch were dissolved in the solvent[20–21] and insoluble petroleum asphaltenes were obtained by pumping and filtration (Fig. S1) with the

yields of asphaltenes being 64%, 80% and 67% for Z1, Z2 and Z3. Asphaltene molecules are mainly composed of aromatic nucleus (125×10^{-6}) as well as aliphatic carbon chains (30×10^{-6}) and oxygen-containing functional groups (138×10^{-6}), as shown in NMR spectra (Fig. 1a and Fig. S2). In contrast, Z2 is rich in aromatic carbon and has the highest oxygen content (2.58%), including more O=C−O groups (Fig. 1b, c). While Z1 and Z3 are primarily composed of chain-structured carbon. The XRD patterns (Fig. 1d and Fig. S2) of the asphaltene materials are fitted with two peaks: the (002) crystal planes at approximately 2θ = 26° correspond to the interlayer spacing of aromatic carbon, while the peak around 2θ = 19° (γ crystal planes) represents the spacing between aliphatic chains[22]. Z1 and Z3 have significantly larger aliphatic chain spacings compared with Z2, indicating a denser arrangement of aliphatic chains. The aromaticity, *F*a (determined by calculating the ratio of the aromatic carbon area and the total area in the fitted spectra)[23], shows that Z2 asphaltene has the highest aromaticity at 0.364, matching well with the above NMR spectra.

Furthermore, Z2 exhibits the lowest average molecular weight, as ascertained through gel permeation chromatography (Table 1). This characteristic contributes to an increased degree of molecular condensation and results in the slowest rate of volatile decomposition (Fig. 1e)[24–25]. The reduction in mass of asphaltenes predominantly takes place within the temperature range of 400 to 600 °C. This phenomenon is primarily ascribed to the cleavage of alkyl side chains, followed by a rearrangement of the carbon framework[26–27]. EPR tests (Fig. 1f) show that the increase in oxygen functional groups in Z2 and the enhancement of spin interactions leads to a slight shift in the *g*-value, although *g* = ~2.003 indicates the nature of the carbon centered radicals[28].

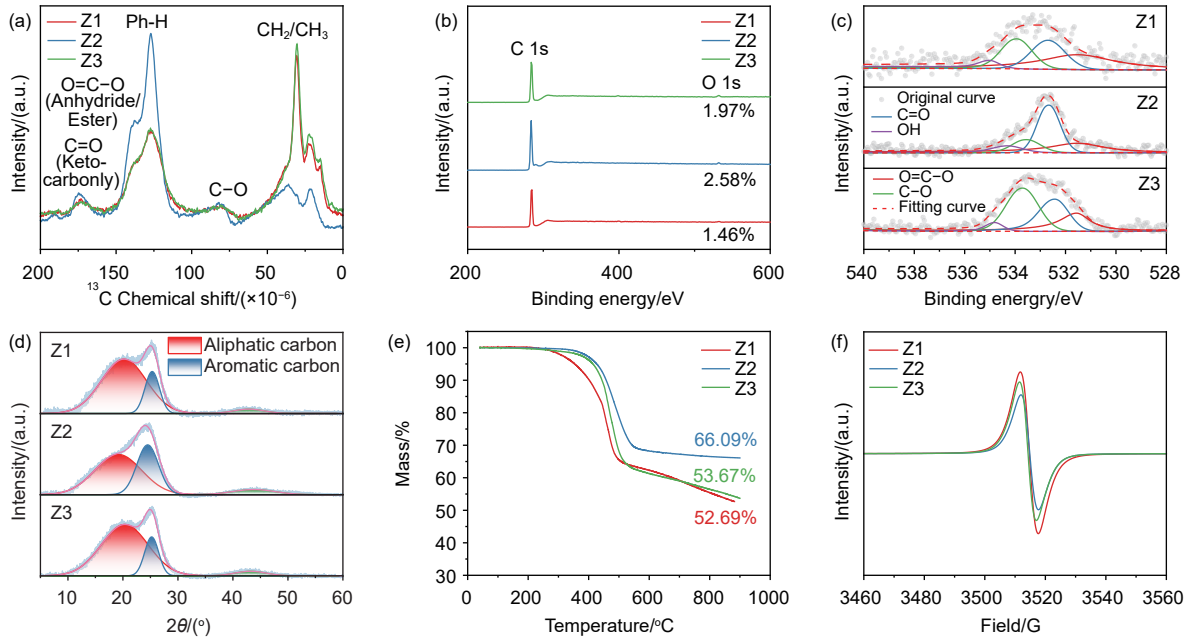

Fig. 1 Structural characterization of asphaltenes feedstocks. (a) ^{13}C NMR spectra. (b) XPS spectra. (c) O 1s XPS spectra. (d) Peak fitting of XRD patterns. (e) TG curves in nitrogen. (f) EPR spectra

Table 1 Analytical characterization of asphaltene feedstocks

Sample	Yield/%	Average molecular weight (GPC)	Chemical composition		*F*a	d_y/nm	*g*-value
			C/%	O/%			
Z1	64	1589	98.13	1.87	0.196	0.436	2.0024
Z2	80	427	97.44	2.56	0.364	0.465	2.0028
Z3	67	1610	98.37	1.63	0.184	0.436	2.0024

3.2 Structural characterizations of pre-oxidized asphaltenes

Pre-oxidation introduces cross-linking structures in asphalt and inhibits rearrangement at high temperatures, enabling the preparation of pitch-based hard carbons[29]. The different structures of pitch precursors determine the degree and mode of molecular cross-linking after pre-oxidation, which in turn affects the production of the microstructure during subsequent high-temperature carbonization[30–31]. Following the pre-oxidation treatment, Z2-300 exhibits a cross-linking structure predominantly characterized by carbonyl (200×10^{-6}) and ester groups (150×10^{-6}), exhibiting a greater concentration of O=C−O group moiety relative to other materials (Fig. 2a). The nearly complete attenuation of chemical shifts associated with $-CH_2/-CH_3$ (30×10^{-6}) suggests that the aliphatic structures experience pyrolysis during the pre-oxidation process, thereby preserving the majority of the aromatic carbon structure. Subsequent XPS analysis (Fig. S3) indicates a substantial increase in the oxygen content on the surface of the material following pre-oxidation, which leads to the formation of additional oxygen-containing functional groups. Notably, the elevated levels of C=O and O=C−O bonds (Table S2, S3) observed in the Z2-300 sample imply the presence of more robust cross-linking structures, attributable to the abundance of polar oxygen-containing functional groups present in the raw material (Fig. 2b, c)[17].

The TG curve of pre-oxidized asphaltene (Fig. S4) reveals significant differences in the thermal decomposition characteristics of pre-oxidized asphaltenes. Notably, the 3D cross-linking structure present in Z2-300, predominantly composed of ester groups, impedes the sliding of carbon layers during the initial stage of pyrolysis. This is attributed to the stabilizing effect of O=C−O bonds, which restricts the movement of carbon layers at the onset temperature of pyrolysis and leads to partial pyrolysis during

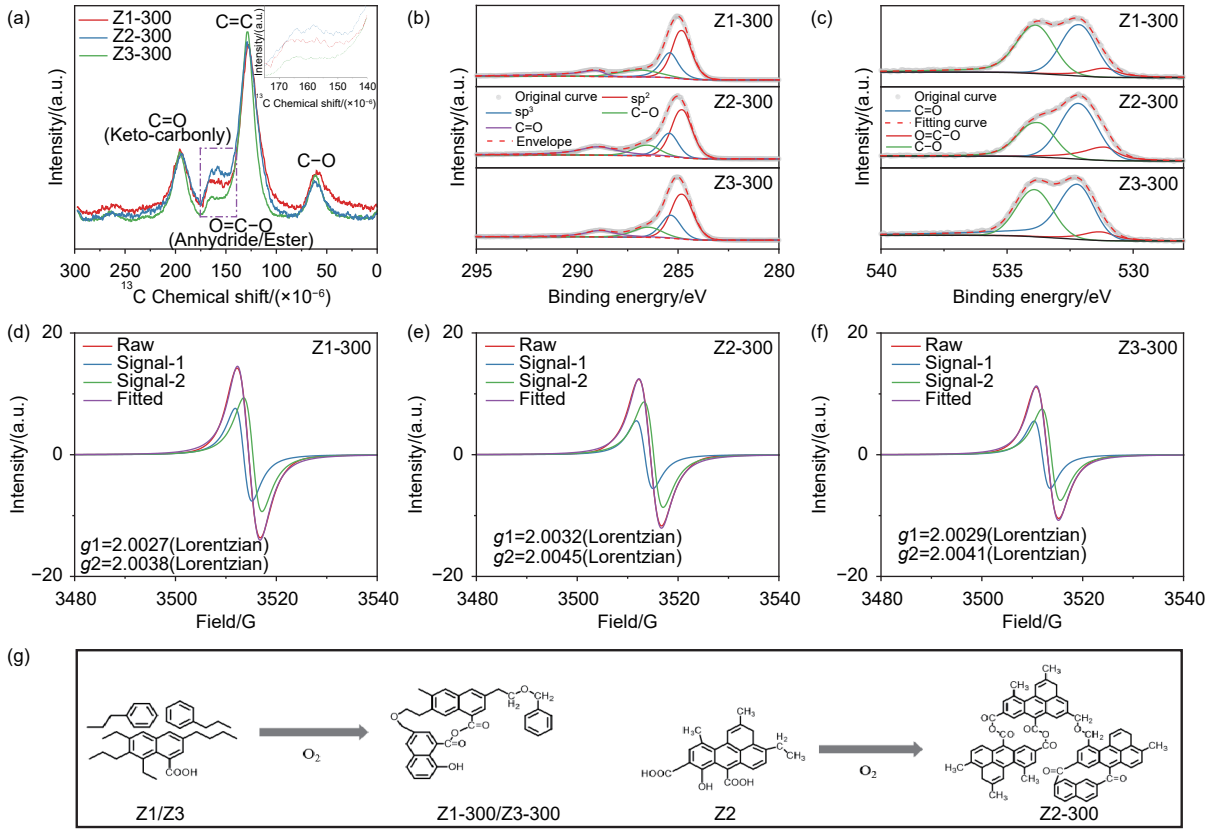

Fig. 2 Pre-oxidation mechanics of asphaltene. (a) ^{13}C NMR spectra of pre-oxidized asphaltene. (b) Fitted XPS C 1s spectra of oxidized asphaltenes. (c) Fitted XPS O 1s spectra of oxidized asphaltene. (d) EPR spectra of Z1-300. (e) EPR spectra of Z2-300. (f) EPR spectra of Z3-300. (g) Mechanism of asphaltene oxidation

the subsequent high-temperature carbonization stage, resulting in the generation of gases and disruption of the graphite layer structure[17]. EPR characterization indicates alterations in free radical characteristics post-pre-oxidation, evidenced by a significant increase in the *g*-value (> 2.0023), which is associated with a higher concentration of oxygen-centered radicals[28]. The Z2-300 sample demonstrates an elevated *g*-value, indicative of enhanced activity of oxygen radicals that are crucial for the reconfiguration of the carbon framework during high-temperature carbonization, and these radicals are effectively retained at the same carbonization temperature[28,32]. Previous research has established that aliphatic carbon chains undergo thermal degradation during the pre-oxidation process, leading to the release of small molecular gases. At increased temperatures, C—O bonds form between adjacent molecules. With prolonged pre-oxidation, there is an incremental incorporation of oxygen, which gradually results in the formation of O=C—O groups and the establishment of a cross-linking structure[23]. Conversely, aromatic carbon groups, characterized by higher degrees of condensation, pose considerable challenges for oxygen functionalization. The limited availability of decomposable alkyl side chains and the extended interatomic distances create steric hindrances that restrict the effective introduction of oxygen-containing functional groups. Even when oxygen is integrated, the steric effects associated with aromatic carbons obstruct the development of a three-dimensional (3D) cross-linking network. In contrast, the Z2 asphaltene contains a higher concentration of oxygen-containing functional groups on its aromatic carbon backbone, facilitating alternative pathways for oxygen incorporation. This process is characterized by interactions between oxygen and aldehydes and ketones in hydroxyl groups to form the corresponding aldehyde or carboxylic acid. Oxidized compounds may undergo further reactions, including esterification, acylation, or decarboxylation, thereby shortening the oxidation stabilization pathways and enhancing oxidative reactivity[33]. Consequently, it can be deduced that the molecular structure of asphaltene undergoes changes during the pre-oxidation process (Fig. 2g): (1) In asphaltene with a high content of aliphatic carbon, the aliphatic carbon chains decompose thermally during pre-oxidation, and oxygen functional groups insert into the aliphatic chains. As oxidation deepens, the oxygen functional groups condense with one another, introducing cross-linking structures into the asphaltene. (2) For oxygen-rich aromatic carbon, the higher reactivity oxygen atoms can react with atmospheric oxygen, disrupting the steric hindrance of aromatic carbon, increasing the probability of oxidative reactions and the degree of crosslinking, and forming a cross-linking structure major composed of ester groups.

3.3 Analysis of asphaltene-derived hard carbon

The unique molecular configurations of asphaltenes demonstrate varying behaviors following the pre-oxidation process, which subsequently influences the microstructure of the resultant hard carbon materials. SEM images illustrate that these hard carbons exhibit an irregular block-like morphology (Fig. 3a-c). In contrast, asphaltenes that undergo direct carbonization reveal a more pronounced layered structure (Fig. S6). This observation suggests that the pre-oxidation process facilitates the formation of cross-linking structures, which inhibit the tendency for graphitization during high-temperature carbonization. HRTEM characterization indicates that all samples display characteristic amorphous features (Fig. S6). Of particular note, the Z2-300-1200 material contains highly disordered and twisted graphite-like layer structures, which arise from the random stacking of bent carbon layers influenced by the cross-linking structures and the steric hindrance effects of the aromatic rings[34–35]. The selected area electron diffraction (SAED) patterns for Z2-300-1200 exhibit more blurred diffraction rings, further corroborating the presence of disordered carbon stacking[36].

Further XRD and Raman spectra tests are performed to reveal the crystallinity characteristics of hard carbons. All hard carbon materials show the amorphous characteristics with the broad peak appearing at 24° ((002) planes for graphite) in the XRD pat-

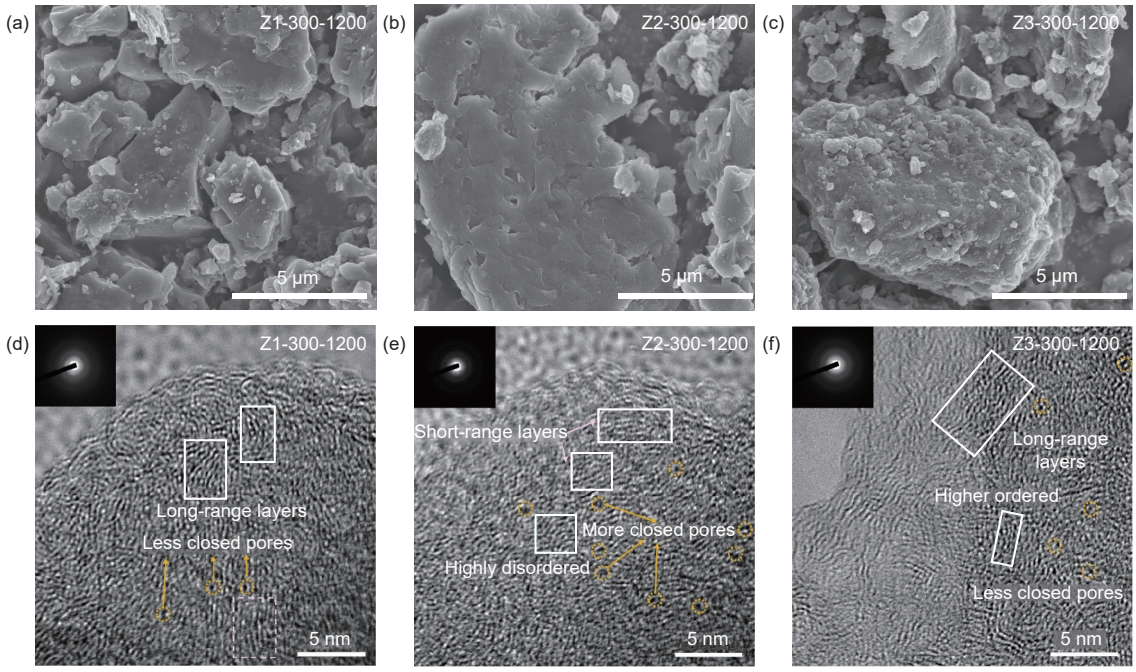

Fig. 3 Morphologies of asphaltene-based hard carbon. (a-c) SEM images of Z1-300-1200, Z2-300-1200 and Z3-300-1200. (d-f) HRTEM images of Z1-300-1200, Z2-300-1200 and Z3-300-1200

terns (Fig. 4a). Notably, the diffraction peak of Z2-300-1200 shows a significant shift with the largest interlayer spacing, as the rigid skeleton formed by aromatic carbon during carbonization prevents the rearrangement of carbon layers[36]. The smaller graphite microcrystals in Z2-300-1200 (Table 2 and Fig. S7) are attributed to the gas generated by the pyrolysis of oxygen-containing functional groups and the disruption of the carbon layers by the rigid carbon framework[35,37]. Furthermore, a sharp peak near 2θ = 44.3° is observed in the XRD pattern of the Z3-300-1200 material, corresponding to the (101) plane of graphite[38]. This peak indicates the formation of more ordered graphitic nanodomains within the carbon structure. Raman spectroscopy can be used to characterize material disorder programs (Fig. 4b). The Raman spectra of hard carbon were deconvoluted into 4 sub-peaks at 1180, 1350, 1500 and 1600 cm^{-1} (Fig. 4d-e), corresponding to the *D*4, *D*1, *D*3 and *G* bands[7]. The Raman analysis indicates that the sample Z2-300-1200 exhibits the highest I_{D1}/I_G ratio of 1.12 and the lowest I_{D3}/I_G ratio of 0.31 (Table S5). This observation implies that the aromatic carbon contributes to the formation of a rigid framework during the carbonization process, thereby restricting the rearrangement of carbon layers and facilitating the development of short-range disordered carbon structures[35]. Concurrently, the ongoing pyrolysis of aliphatic carbon results in the introduction of additional defect sites within the graphite layers[23,39].

XPS analysis indicates that the hard carbon surface retains a significant amount of oxygen-containing functional groups (Fig. S9), while Z2-300-1200 shows a higher proportion of C=O functions, which is favorable for the reversible adsorption of sodium ions. EPR analysis indicates that both Z1-300-1200 and Z3-300-1200 show minimal response, whereas Z2-300-1200 presents a weak and broad peak at *g*=2.0040 with a linewidth of 132.4 G (Fig. 4c). This observation aligns with our earlier findings, suggesting that hard carbon materials exhibiting plateau capacity tend to have weak EPR signals, with the spins adhering to Pauli's law[40]. The radicals responsible for these signals are likely derived from graphite microcrystals and its delocalized electrons[41], which constitute the pore walls of the closed pore structures in hard carbon. In these graphite microcrystals, mobile electrons are restricted compared with those in the continuous aromatic structure of graphite[41]. Moreover, the EPR signal of Z2-300-1200 reveals the

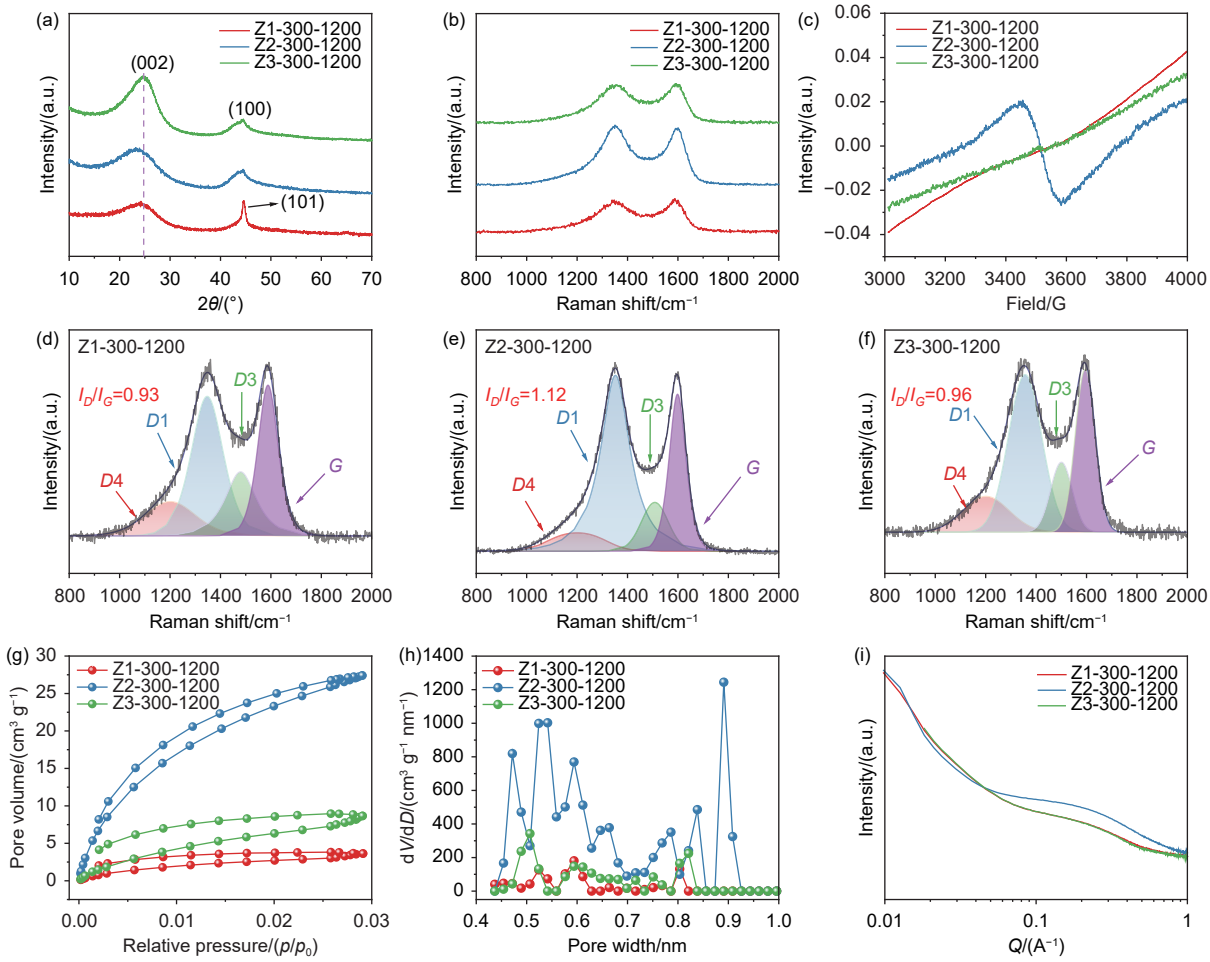

Fig. 4 Structural analysis of asphaltene-based derived hard carbon. (a) XRD patterns. (b) Raman spectra. (c) EPR spectra of hard carbons. (d-f) Raman peak splitting fitting results. (g) CO_2 adsorption isotherms. (h) Pore size distribution. (i) SAXS patterns

Table 2 Structural parameters of hard carbons

Sample	d_{002}/(Å)	L_c/(nm)	L_a(nm)	R	I_{D1}/I_G	O/%	S_{CO_2}(BET)/(m^2 g^{-1})	B (SAXS)
Z1-300-1200	3.69	1.19	4.16	2.87	0.93	5.14	9.35	0.029
Z2-300-1200	3.78	1.04	1.70	1.84	1.12	7.11	84.45	0.099
Z3-300-1200	3.71	1.10	2.05	2.90	0.98	4.72	9.44	0.026

presence of intrinsic carbon defects. Unlike the sharp EPR response produced by sigma dangling bonds, which adhere to the Curie-Weiss law[42], these intrinsic defects increase the graphite microcrystalline electronic band gap and promote the emergence of new energy bands, modulating the charge density and favoring the adsorption of sodium between graphite layers[43]. This improvement in the electronic structure could, in turn, enhance the kinetics of sodium storage[44]. The N_2 adsorption-desorption isotherm indicates the existence of a significant amount of micropores, along with a small number of mesopores (Fig. S10). The N_2-BET surface area exhibits relatively low values (<100 m^2 g^{-1}), which is consistent with the typical characteristics of hard carbon reported in the literature[45–46]. CO_2 adsorption-desorption (Fig. 4g) further reveals that the material contains a substantial amount of closed pore structures, with Z2-300-1200 having the highest content. The pore sizes predominantly locate in the range between 0.4 and 0.9 nm, which serve as crucial storage sites for sodium ions[23]. The closed pore structure of the material was investigated using SAXS (Fig. 4i), where the material displays a high-intensity scattering plateau, indicating a well-developed internal closed pore structure. Notably, the higher scattering peak appears near 0.1 Å^{-1}

in Z2-300-1200, suggesting the presence of more closed pores. The fitting results of SAXS (Fig. S11) indicate that Z2-300-1200 has a higher B value (number of closed pores), suggesting a more abundant closed pore structure, which correlates well with its larger specific surface area (Fig. 4h)[46–47]. The characterization results demonstrate that during the carbonization of pitch, oxygen-containing functional groups experience a gradual thermal decomposition, leading to the release of small gaseous molecules such as CO_2, H_2O and CH_4. This decomposition process facilitates the creation of free volume within the material. The formation of aromatic rings, which establish a rigid framework during carbonization, contributes to the conversion of free volume into closed pores due to their steric hindrance effects. Furthermore, the spatial constraints imposed by these aromatic structures encourage a disordered rearrangement of the rigid carbon skeleton at elevated temperatures, ultimately resulting in the gradual formation of smaller graphite microcrystals. The stacking of these bent and disordered graphite microcrystals plays a significant role in the development of closed pore structures. Conversely, precursors with a higher aliphatic carbon content do not provide adequate rigid chain support during high-temperature carbonization, thereby complicating the transformation of free volume into closed volume. This limitation leads to an increased number of defect sites within the graphite layers, a finding that is corroborated by the Raman peak deconvolution analysis.

3.4 Electrochemical sodium-ion storage mechanism

Previous research indicates that the varying structures of asphaltene precursors significantly affect the level of disorder and the pore architecture of the resultant material. Subsequently, the synthesized asphaltene-based hard carbon is employed as an anode in SIBs to assess its electrochemical performance[28,33]. The GCD curves for the asphaltene-derived hard carbons are illustrated in Fig. 5(a–c) (Z1-300-1200, Z2-300-1200, Z3-300-1200).

Considering the effect of the irreversible solid electrolyte interphase (SEI) formation, we used the discharge curve from its second cycle to evaluate the sodium storage capacity. The obtained hard carbon anode delivers the discharge capacity of 262.61, 333.13 and 267.06 mAh g^{-1}, following the initial coulombic efficiency (ICE) values of 62.00%, 63.41% and 64.33% for Z1-300-1200, Z2-300-1200 and Z3-300-1200, respectively[48]. However, the low ICE is attributed to the large specific surface area (N_2 BET, Fig. S11) exposed to the electrolyte and the edge-defective structure[48], including oxygen-containing functional groups (XPS in Fig. S10). Effective strategies may include defect repairing under hydrogen reduction[49] and pre-sodiation treatment[50]. We have employed a pre-sodiation method to enhance the ICE of the material and assembled full batteries (Fig. S15). To further demonstrate the superiority of the Z2 structure, we analyze the sloping and plateau capacities (Fig. 5g). The slope capacities of the materials are 133.14, 149.54, and 127.03 mAh g^{-1} for Z1-300-1200 Z2-300-1200 and Z3-300-1200, respectively. Comparatively, Z2 hard carbon possesses a larger accessible surface exposed to the electrolyte (supported with the higher N_2-BET value) and an abundance of C=O functional groups. These characteristics facilitate the adsorption and storage of sodium ions, thus leading to higher sloping capacity. The plateau capacities are 129.47, 183.59 and 140.03 mAh g^{-1} for Z1-300-1200 Z2-300-1200 and Z3-300-1200, respectively. As widely reported in the literature, the rich closed pore characteristics and larger interlayer spacing in Z2-300-1200 hard carbon facilitates the pore-filling and insertion processes of sodium ions, thus resulting in a higher plateau capacity. The reduction peak appeared at a potential of ca. 1.2 V during its first CV (Fig. 5c, Fig. 5d, and Fig. 5f) is attributed to side reactions related to the formation of the SEI layer[7]. The redox peaks near 0.1 V correspond to the filling-extraction of sodium ions in closed pores. Notably, Z2-300-1200 exhibits the sharpest redox peaks[51], indicating the enhanced sodium ion filling-extraction rates in closed pores, which demonstrates its structural advantage in plateau capacity[52–53]. Anodic and broad cathodic peaks of higher current intensity were observed in the

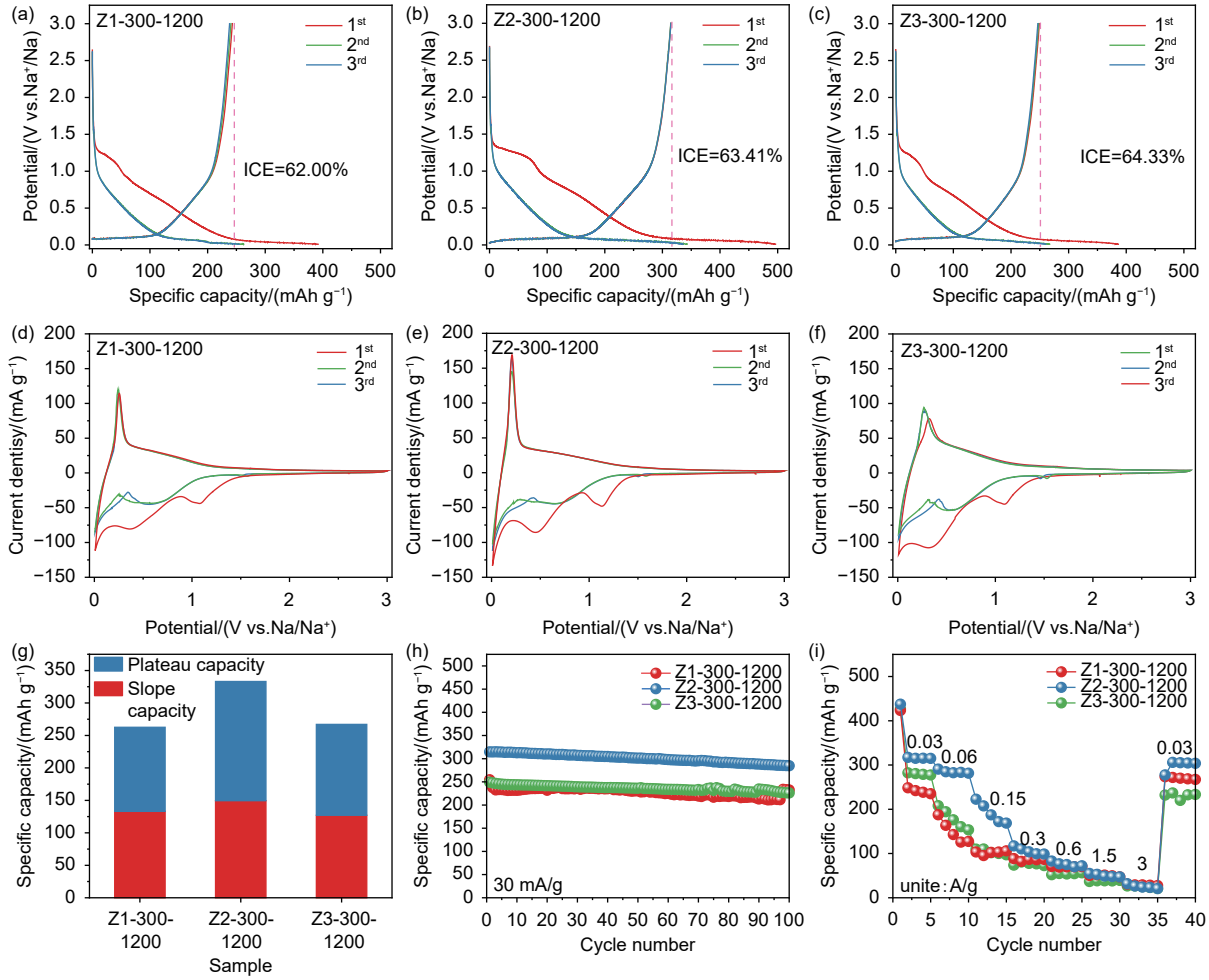

Fig. 5 Electrochemical properties of asphaltene-derived hard carbons. GCD curves at 30 mA g^{-1} and initial CV profiles at a scan rate of 0.1 mV s^{-1} for (a, d) Z1-300-1200, (b, e) Z2-300-1200 and (c, f) Z3-300-1200. (g) Capacity contribution of the slop region and plateau region in the second cycle sodiation curve. (h) Material cycling performance. (i) Material rate performance

higher potential region of the CV curve (0.5–1.2 V). These peaks indicate sodium-ion adsorption at the defects within the graphite interlayers, corresponding to the slope capacity.

Fig. 5h illustrates the cycling performance of the Zx-300-1200 at 0.1 C. All tested samples exhibit excellent capacity retention, with the retentions of 91.32%, 94.51% and 90.74% after 100 cycles at 30 mA g^{-1} for Z1-300-1200, Z2-300-1200 and Z3-300-1200, respectively. Notably, with a slight decay in capacity, Z2-300-1200 delivered the highest reversible specific capacity of 316.7 mAh g^{-1}. Z2-300-1200 exhibits structural superiority with higher capacity and lower production cost compared to other pitch-based disordered carbon materials (Table S9). Fig. 5g shows the rate capability performances of anode materials, ranging from 0.1 C to 5 C. The reduced sodium storage capability is attributed to the limited diffusion rate of sodium ions within the hard carbon, which hinders efficient utilization of the plateau sodium storage site under large current conditions, causing the sloping capacity to dominate (Fig. S15). Fortunately, when the current density returns to 30 mA g^{-1}, the reversible capacity of Z2-300-1200 recovers, indicating that the carbon structure of the material is robust and exhibits good reversibility.

To further investigate the sodium-ion storage mechanism of asphaltene based hard carbon anodes, kinetic performance tests are conducted. As the scanning rate increases, the peak current progressively intensifies, with the P peak shifted slightly toward a higher potential[54]. The potential difference between the redox peaks of Z2-300-1200 increases significantly, while the overall shape of the CV curve is well

preserved, indicating enhanced reversibility and stability. The rate of their reaction kinetics can be assessed by calculating the *b* values of the corresponding oxidation–reduction peaks according to equation $i = av^b$. The *b* values are 0.724 and 0.786 (for peak P) in the low-potential region, showing that sodium-ion storage behavior of the plateau region is the result of a synergistic effect between diffusion-controlled processes and surface capacitive reactions. In contrast, the *b* values are 0.954 and 0.972 (for peak S) in the high-potential region, suggesting that the storage process in the sloping region is predominantly capacitive-controlled[55]. The calculated contributions of diffusion-controlled and capacitive-controlled processes (Fig. 6d, f) demonstrate that capacitive controlled contribution increases with scan rate, and Z2-300-1200 has a higher proportion of pseudo capacitance at various scan rates. This suggests that the rich C=O functional groups and various surface defects in Z2-300-1200 can synergistically enhance sodium-ion adsorption, accelerate electrode reaction kinetics, and increase the pseudocapacitive contribution[56].

By fitting the EIS results (Fig. 5i), it can be counted that the charge transfer resistance (R_{ct}) of all 3 materials is the approximately same. However, the abundant porous structure of Z2-300-1200 facilitates sodium ion transport, resulting in the lowest diffusion resistance, highlighting its superior kinetic performance. The GITT was further used to analyze the reaction kinetics of the materials. Fig. 6j shows the discharge process of the 3 materials, while Fig. 6k illustrates the relationship between ion mobility and voltage. During the discharge process, the ion mobility of all 3 materials decreases as the voltage increases. Z2-300-1200 demonstrates relatively high ion mobility, where sodium ions adsorb on the surface of hard carbon and gradually diffuse into the interlayers. The speedy diffusion kinetics of sodium ions contribute to better high-rate performance. When the voltage drops below 0.1 V, the sodium storage sites within the interlayers become fully occupied, and the ion mobility sharply decreases. At this stage, sodium ions

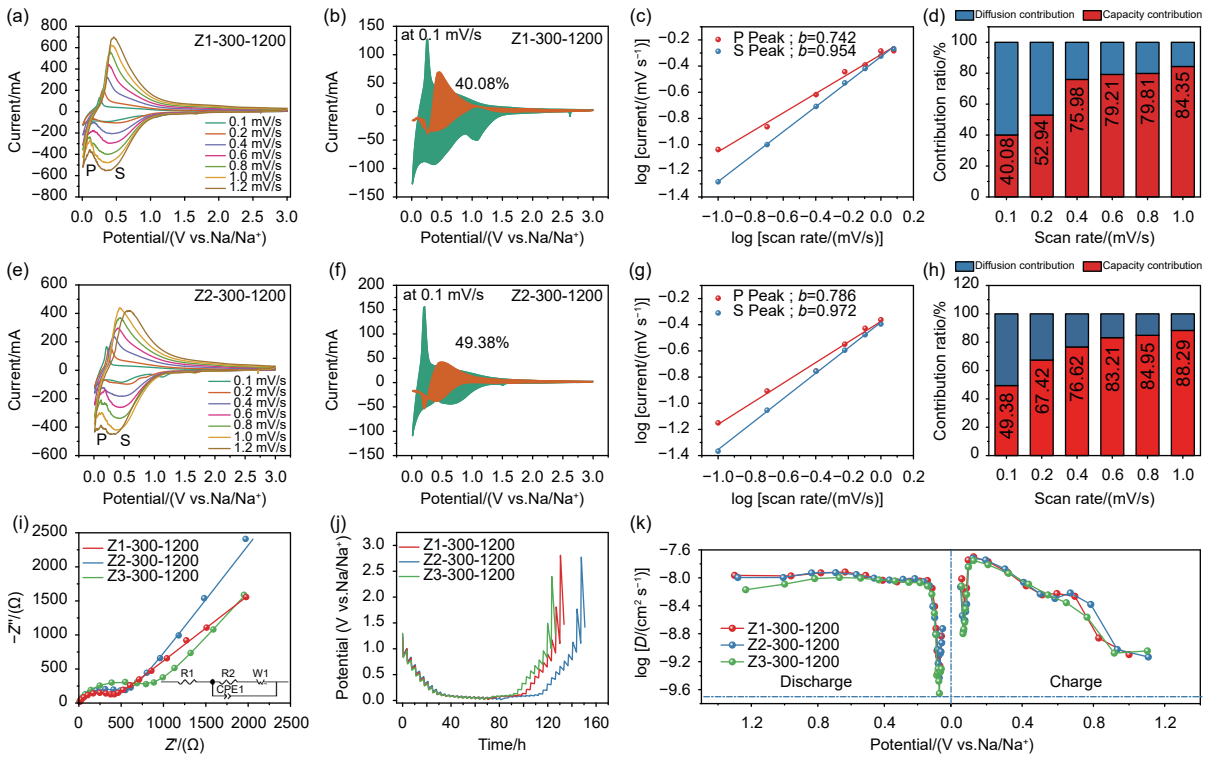

Fig. 6　Kinetic analysis. (a-d) CV curves at different scan rates; 0.1 mV s^{-1} CV curve with the capacitive contribution; The linear relationship between log*i* and log*v*; Normalized contribution ratio of capacitive capacities at different scan rates of Z1-300-1200. (e-h) CV curves at different scan rates; 0.1 mV s^{-1} CV curve with the capacitive contribution; The linear relationship between log*i* and log*v*; Normalized contribution ratio of capacitive capacities at different scan rates of Z2-300-1200. (i) Nyquist plots. (j) GITT potential profiles curves. (k) Sodium-ion apparent diffusion coefficients

primarily reside in micropores, which impedes rapid diffusion. However, as the voltage decreases to below 0.05 V, the ion diffusion rate of Z2-300-1200 significantly increases, indicating that its rich closed pore structure enables sodium ions to be adsorbed and clustered within the pores, which serve as the major contributor to the low-voltage plateau capacity[57]. The sodium ion diffusion rates during the charging process are similar to those observed during discharge, demonstrating highly reversible sodium-ion storage processes.

4 Conclusions

The structural evolution of different molecular components of pitch under thermochemical treatment is a key factor influencing the sodium-ion storage performance of pitch-based hard carbon anodes. Based on molecular structural characterization, we investigated the mechanism by which air pre-oxidation treatment influences the interaction between aromatic rings and aliphatic chains. In addition, the existence of polar oxygen functional groups can overcome the steric hindrance posed by aromatic rings, thereby facilitating the introduction of additional cross-linking structures. In contrast, aromatic rings form a rigid carbon skeleton during high-temperature carbonization, and their steric effects can suppress the rearrangement of carbon layers, leading to the generation of short-range disordered carbon layer structures that promote the formation of closed pore architectures. Consequently, the graphite nanodomain structure of Z2-300-1200 is more disordered, with a richer closed pore structures, which favors sodium storage in the plateau region. Z2-300-1200 exhibited a high reversible capacity of 316.7 mAh g^{-1} and excellent stability, demonstrating its potential for use in SIBs. Our findings provide a theoretical basis for the selection of upstream raw materials for the development of high-quality pitch-based hard carbon materials.

Declaration of competing interest

The authors declare that they have no known competing financial interests or personal relationships that could have appeared to influence the work reported in this paper.

Acknowledgements

This work was financially supported by the National Natural Science Foundation of China (22309206, 22179145, 21975287 and 22138013), National Key Research and Development Program (2023YFB4203702, 2023YFB4203703) Shandong Provincial Natural Science Foundation (ZR2020ZD08), Taishan Scholars Program of Shandong Province (tsqn20221117), Shandong Provincial Excellent Young Scientists Fund Program (Overseas) (2024HWYQ-047), National Natural Science Foundation of Qingdao (23-2-1-24-zyyd-jch).

References

[1] Hwang J Y, Myung S T, Sun Y K, Sodium-ion batteries: present and future[J]. Chemical Society Reviews, 2017, 46: 3529–3614.

[2] Dou X, Hasa I, Saurel D, et al. Hard carbons for sodium-ion batteries: Structure, analysis, sustainability, and electrochemistry[J]. Materials Today, 2019, 23: 87-104.

[3] Li Q, Liu X S, Tao Y, et al. Sieving carbons promise practical anodes with extensible low-potential plateaus for sodium batteries[J]. National Science Review, 2022, 9: nwac084.

[4] Wu J R, Yang T, Song Y, et al. Preparation of disordered carbon for alkali metal-ion (Lithium, Sodium, and Potassium) batteries by pitch molecular modification: A review[J]. Carbon, 2024, 221: 118902.

[5] Meng Q, Chen B, Jian W B, et al. Hard carbon anodes for sodium-ion batteries: Dependence of the microstructure and performance on the molecular structure of lignin[J]. Journal of Power Sources, 2023, 581: 233475.

[6] Li F, Mei R G, Wang N, et al. Regulating the closed pore structure of biomass-derived hard carbons towards enhanced sodium storage[J]. Carbon, 2024, 230: 119556.

[7] Chen H, Sun N, Wang Y X, et al. One stone two birds: Pitch assisted microcrystalline regulation and defect engineering in coal-based carbon anodes for sodium-ion batteries[J]. Energy Storage Materials, 2023, 56: 532-541.

[8] Kamiyama A, Kubota K, Igarashi D, et al. MgO-template synthesis of extremely high capacity hard carbon for Na-ion battery[J]. Angewandte Chemie-International Edition, 2021, 60: 5114-5120.

[9] Zhang Q T, Shu Q Q, Liang C L, et al. F, O co-doped porous hard carbon from conjugated microporous polymer for efficient lithium storage[J]. Journal of Electroanalytical Chemistry, 2024, 964: 118355.

[10] Yao Y Z, Wan Y, Li Y N, et al. Precursor chemistry-mediated defect regulation of asphalt-derived carbonaceous materials for slope-dominated sodium storage[J]. Journal of Alloys and Compounds, 2022, 928: 167103.

[11] Guo N N, Liu A J, Luo W X, et al. Hybrid nanoarchitectonics of coal-derived carbon with oxidation-induced morphology-selectivity for high-performance supercapacitor[J]. Journal of Colloid and Interface Science, 2023, 639: 171-179.

[12] Wang J, L Yan, Liu B H, et al. A solvothermal pre-oxidation strategy converting pitch from soft carbon to hard carbon for enhanced sodium storage[J]. Chinese Chemical Letters, 2023, 34: 107526.

[13] He H N, He J, Yu H B, et al. Dual-interfering chemistry for soft-hard carbon translation toward fast and durable sodium storage[J]. Advanced Energy Materials, 2023, 13: 2300357.

[14] Yin X P, Zhao Y F, Wang X, et al. Modulating the graphitic domains of hard carbons derived from mixed pitch and resin to achieve high rate and stable sodium storage[J]. Small, 2022, 18: 2105568.

[15] Zhang C, Yang J, Xue Y, et al. Group type analysis of asphalt by column liquid chromatography[J]. Petroleum Science and Technology, 2008, 26: 665-673.

[16] Zhang Y, Fang H Q, Guan L, et al. Effect of asphalt component distribution characteristics in layered porous carbon on performance of supercapacitors[J]. Journal of Power Sources, 2024, 593: 233966.

[17] Xu R, Yi Z L, Song M X, et al. Boosting sodium storage performance of hard carbons by regulating oxygen functionalities of the cross-linked asphalt precursor[J]. Carbon, 2023, 206: 94-104.

[18] Yang T, Song Y, Tian X D, et al. Insight into pore structures evolution and applications in lithium-sulfur battery of pitch fractions-based activated carbons[J]. Journal of Alloys and Compounds, 2021, 875: 160067.

[19] Wang L B, Xu Z K, Lin P, et al. Oxygen-crosslinker effect on the electrochemical characteristics of asphalt-based hard carbon anodes for sodium-ion batteries[J]. Advanced Energy Materials, 2024: 2403084.

[20] Wang, Y W, Cheng T X, Zhou G D. Structural characteristics and interfacial properties of n-hexane and n-heptane-asphaltenes[J]. Petroleum Chemistry, 2022, 62: 740-751.

[21] Alostad L K, Palacio Lozano, Gannon B, et al. Investigating the influence of n-heptane versus n-nonane upon the extraction of asphaltenes[J]. Energy Fuels, 2022, 36: 8663-8673.

[22] AlHumaidan F S, Hauser A, Rana M S, et al. Changes in asphaltene structure during thermal cracking of residual oils: XRD study[J]. Fuel, 2015, 150: 558-564.

[23] Zhao G X, Xu T Q, Zhao Y M, et al. Conversion of aliphatic structure-rich coal maceral into high-capacity hard carbons for sodium-ion batteries[J]. Energy Storage Materials, 2024, 67: 103282.

[24] Fanjul F, Granda M, Santamaría R, et al. On the chemistry of the oxidative stabilization and carbonization of carbonaceous mesophase[J]. Fuel, 2002, 81: 2061-2070.

[25] Qi M Y, Huang S, Baker N, et al. Correlation of mesophase properties with molecular structures of pitches from different sources[J]. Energy Fuels, 2024, 38: 2855-2865.

[26] Hauser A, Bahzad D, Stanislaus A, et al. Thermogravimetric analysis studies on the thermal stability of asphaltenes: Pyrolysis behavior of heavy oil asphaltenes[J]. Energy Fuels, 2008, 22: 449-454.

[27] Boytsova A, Kondrasheva N, Ancheyta J, Thermogravimetric determination and pyrolysis thermodynamic parameters of heavy oils and asphaltenes[J]. Energy Fuels, 2017, 31: 10566–10575.

[28] Wang B, Yao Y Z, Wang W L, et al. Resolution of the reciprocity between radical species from precursor and closed pore formation in hard carbon for sodium storage[J]. Journal of Colloid and Interface Science, 2024, 664: 681-690.

[29] Lu Y X, Zhao C L, Qi X G, et al. Pre-oxidation-tuned microstructures of carbon anodes derived from pitch for enhancing Na storage performance[J]. Advanced Energy Materials, 2018, 8: 1800108.

[30] Zhu Y H, Tian F, Liu Y Q, et al. Comparison of the composition and structure for coal-derived and petroleum heavy subfraction by an improved separation method[J]. Fuel, 2021, 292: 120362.

[31] Guan T T, Zhang G L, Zhao J H, et al. Insight into the oxidative reactivity of pitch fractions for predicting and optimizing the oxidation stabilization of pitch[J]. Fuel, 2019, 242: 184-194.

[32] Wang B, Yao Y Z, Wang W L, et al. Identifying the plateau sodium storage behavior of hard carbon through the spin state[J]. Chemical Engineering Journal, 2024, 488: 151055.

[33] Zhang X F, Yi Z L, Tian Y R, et al. Insight into the effect of structural differences among pitch fractions on sodium storage performance of pitch-derived hard carbons[J]. Carbon, 2024, 226: 119165.

[34] Yan B T, Han C, Dai Y M, et al. Biomass derived hard carbon materials for sodium ion battery anodes: Exploring the influence of carbon source on structure and sodium storage performance[J]. Fuel, 2024, 371: 132141.

[35] Lin J H, Zhou Q F, Liao Z S, et al. Steric hindrance engineering to modulate the closed pores formation of polymer-derived hard carbon for high - performance sodium-ion batteries[J]. Angewandte Chemie-International Edition, 2024, 63: e202409906.

[36] Zhou H Y, Sun N, Yu J X, et al. Microstructure regulation of resin-based hard carbons via esterification cross-linking for high-performance sodium-ion batteries[J]. Inorganic Chemistry Frontiers, 2023, 10: 2404-2413.

[37] Zhao B Y, Li X T, Shang L, et al. Regulating oxygen functionalities of cellulose-derived hard carbon toward superior sodium storage[J]. Journal of Materials Chemistry A, 2024, 12: 5834-5845.

[38] Huang P, Liu B, Zhang Z L, et al. Silicon/carbon composites based on natural microcrystalline graphite as anode for lithium-ion batteries[J]. Ionics, 2021, 27: 1957-1966.

[39] Xue S S, Li P F, Sun L, et al. The Formation Process and Mechanism of Carbon Dots Prepared from Aromatic Compounds as Precursors: A Review[J]. Small, 2023, 19: 2206180.

[40] Insinna T, Bassey E N, Märker K, et al. Graphite anodes for Li-Ion batteries: An electron paramagnetic resonance investigation[J]. Chemistry of Materials, 2023, 35: 5497-5511.

[41] Wang B, Fitzpatrick J R, Brookfield A, et al. Electron paramagnetic resonance as a tool to determine the sodium charge storage mechanism of hard carbon[J]. Nature Communications, 2024, 15: 3013.

[42] Wang B, Fielding A J, Dryfe R A W, Electron paramagnetic resonance as a structural tool to study graphene oxide: Potential dependence of the EPR response[J]. Journal of Physical Chemistry C, 2019, 123: 22556–22563.

[43] Guo R Q, Lv C X, Xu W J, et al. Effect of intrinsic defects of carbon materials on the sodium storage performance[J]. Advanced Energy Materials, 2020, 10: 1903652.

[44] Li Y Q, Vasileiadis A, Zhou Q, et al. Origin of fast charging in hard carbon anodes[J]. Nature Energy, 2024, 9: 134-142.

[45] Sun D, Zhao L, Sun P L, et al. Rationally regulating closed pore structures by pitch coating to boost sodium storage performance of hard carbon in low-voltage platforms[J]. Advanced Functional Materials, 2024, 34: 2403642.

[46] Li X, Sun N, Zhang S S, et al. Closed pore structure engineering from ultra-micropores with the assistance of polypropylene for boosted sodium ion storage[J]. Journal of Materials Chemistry A, 2024, 12: 12015-12025.

[47] Wang Y L, Yi Z L, Xie L J, et al. Releasing free radicals in precursor triggers the formation of closed pores in hard carbon for sodium-ion batteries[J]. Advanced Materials, 2024, 36: 2401249.

[48] Gao Y F, Design of hard carbon anode with low specific surface area and low porosity in sodium ion battery[J]. IOP Conference Series: Earth and Environmental Science, 2021, 804: 032025.

[49] Song M X, Yi Z L, Xu R, et al. Towards enhanced sodium storage of hard carbon anodes: Regulating the oxygen content in precursor by low-temperature hydrogen reduction[J]. Energy Storage Materials, 2022, 51: 620-629.

[50] Liu M C, Zhang J Y, Guo S H, et al. Chemically presodiated hard carbon anodes with enhanced initial coulombic efficiencies for high-energy sodium ion batteries[J]. ACS Applied Materials & Interfaces, 2020, 12: 17620-17627.

[51] Li J, Zheng H, Du B D, et al. Preparation of hard–soft carbon via Co-carbonization for the enhanced plateau capacity of sodium-ion batteries[J]. Energy Fuels, 2024, 38: 13398-13406.

[52] Hasegawa G, Kanamori K, Kannari N, et al. Hard carbon anodes for Na-ion batteries: Toward a practical use in[J]. Chemelectrochem, 2015: 1917–1920.

[53] Suo L Y, Zhu J H, Shen X Y, et al. Hard carbon spheres interconnected by carbon nanotubes as high-performance anodes for sodium-ion batteries[J]. Carbon, 2019, 151: 1-9.

[54] Sheng L, Wei P, Ma H, et al. A molecular-scale regulation strategy for designing asphalt-based hard carbon for superior sodium storage[J]. Journal of Materials Chemistry A, 2024, 12: 31480-31491.

[55] Zhao H Q, Chang G B, Gao X M, et al. Fe catalysed transformation of oxygen functional groups on coal based needle coke for sodium storage[J]. Carbon, 2023, 203: 68-75.

[56] Xu T Y, Qiu X, Zhang X, et al. Regulation of surface oxygen functional groups and pore structure of bamboo-derived hard carbon for enhanced sodium storage performance[J]. Chemical Engineering Journal, 2023, 452: 139514.

[57] Kitsu Iglesias L, Antonio E N, Martinez T D, et al. Revealing the sodium storage mechanisms in hard carbon pores[J]. Advanced Energy Materials, 2023, 13: 2302171.